Icarus 276 (2016) 170–181

Contents lists available at ScienceDirect

Icarus

journal homepage: www.elsevier.com/locate/icarus

The gravitational signature of internal flows in giant planets: Comparing the thermal wind approach with barotropic potential-surface methods

Y. Kaspi [a,*], J.E. Davighi [a,b], E. Galanti [a], W.B. Hubbard [c]

[a] Department of Earth and Planetary Sciences, Weizmann Institute of Science, Rehovot, Israel
[b] Department of Physics, University of Cambridge, Cambridge, UK
[c] Lunar and Planetary Laboratory, University of Arizona, Tucson, AZ, USA

ARTICLE INFO

Article history:
Received 23 August 2015
Revised 31 March 2016
Accepted 5 April 2016
Available online 26 April 2016

Keywords:
Jupiter, atmosphere
Jupiter, interior
Atmospheres, dynamics

ABSTRACT

The upcoming Juno and Cassini gravity measurements of Jupiter and Saturn, respectively, will allow probing the internal dynamics of these planets through accurate analysis of their gravity spectra. To date, two general approaches have been suggested for relating the flow velocities and gravity fields. In the first, barotropic potential surface models, which naturally take into account the oblateness of the planet, are used to calculate the gravity field. However, barotropicity restricts the flows to be constant along cylinders parallel to the rotation axis. The second approach, calculated in the reference frame of the rotating planet, assumes that due to the large scale and rapid rotation of these planets, the winds are to leading order in geostrophic balance. Therefore, thermal wind balance relates the wind shear to the density gradients. While this approach can take into account any internal flow structure, it is limited to only calculating the dynamical gravity contributions, and has traditionally assumed spherical symmetry. This study comes to relate the two approaches both from a theoretical perspective, showing that they are analytically identical in the barotropic limit, and numerically, through systematically comparing the different model solutions for the gravity harmonics. For the barotropic potential surface models we employ two independent solution methods – the potential-theory and Maclaurin spheroid methods. We find that despite the sphericity assumption, in the barotropic limit the thermal wind solutions match well the barotropic oblate potential-surface solutions.

1. Introduction

In July 2016, the Juno spacecraft will arrive at Jupiter, on course for a highly eccentric polar orbit of the planet. One of the primary goals of the mission is to perform high sensitivity gravity measurements, with expected sensitivity being at least up to gravity harmonic J_{10} (Bolton, 2005; Finocchiaro and Iess, 2010). These gravity measurements can be used for constraining the planet's internal structure, as well as its atmospheric and interior dynamics (Hubbard, 1999; Kaspi et al., 2010). In particular, these measurements may be able to address one of the longest-standing questions in planetary atmospheric dynamics: to what depth do the observed strong east-west jet-streams on Jupiter penetrate? Soon after the arrival of Juno at Jupiter, the Cassini spacecraft will begin its final proximal orbits prior to its decent into Saturn, mimicking a Juno-like eccentric orbit with close flybys of the cloud-level winds (Spilker et al., 2014). These proximal orbits will facilitate the same type of gravity analysis for Saturn. Thus, in the next couple of years the gravity spectra of both Jupiter and Saturn will be improved by several orders of magnitude, which can be used to potentially advance our understanding of the internal structure, atmospheric dynamics and origin of these planets. The goal of this study is to establish a unified framework in which to analyze these gravity measurements.

1.1. The zonal flow on Jupiter and Saturn

Both Jupiter and Saturn are characterized by strong east-west zonal flows at their observed cloud-level. Jupiter has at least six jets in each hemisphere with maximum wind velocities reaching 140 m s^{-1} at latitude 20°N relative to the System III spin rate (Porco et al., 2003). The equatorial region is flowing eastward with wind speeds exceeding 100 m s^{-1} (Fig. 1). Saturn has a broader wind structure around the equator with the eastward superrotating

* Corresponding author. Tel.: +972 89344238.
E-mail address: yohai.kaspi@weizmann.ac.il (Y. Kaspi).

http://dx.doi.org/10.1016/j.icarus.2016.04.001
0019-1035/

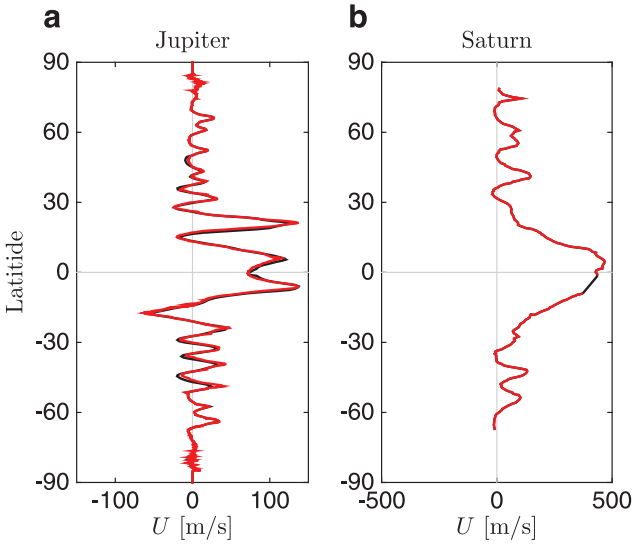

Fig. 1. Zonal mean wind profile (m s^{-1}) as function of latitude for Jupiter (Porco et al., 2003) (left) and Saturn (Sánchez-Lavega et al., 2000) (right). Shown are the observations (red), and the profiles used in the calculations (black) where gaps were filled, and some smoothing applied. (For interpretation of the references to color in this figure legend, the reader is referred to the web version of this article.)

winds reaching nearly latitude 30° in both hemispheres, and wind velocities of over 400 m s^{-1} (Sánchez-Lavega et al., 2000, 2003). For both planets these observations are obtained by cloud tracking of features within the cloud-level, and therefore the measurements are limited to the level of the cloud-motion, roughly between 0.1 and 1 bars (Vasavada and Showman, 2005).

The only direct observation of sub-cloud level winds comes from the Galileo probe that descended into the planet in 1995, and showed, at that location (6°N), an increase in zonal velocity from 80 m s^{-1} at the 1 bar level to 160 m s^{-1} at the 4 bar level, and then a constant wind speed down to the 24 bar level where the probe was lost (Atkinson et al., 1996). However the probe entered a "hot spot" which may not be a good representation of the general flow (Orton et al., 1998; Showman and Dowling, 2000). Indirect observations of the sub-cloud level winds using cloud tracked wind velocities have been inferred by Dowling and Ingersoll (1988, 1989), who suggest based on arguments of conservation of potential vorticity (Pedlosky, 1987) that there must be nonzero zonal winds underlying the Great Red Spot. Conrath et al. (1981) and Gierasch et al. (1986) use thermal-wind arguments to show that deep winds are expected beneath the cloud level. However these deductions are limited to less than the outer 1% of the radius of the planet, and therefore do not infer much about the deep winds. Modeling studies have been wide-spread regarding whether the flow is sheared beneath the cloud level. Suggested mechanisms for a radial shear with depth include compressible effects (Kaspi et al., 2009) and magnetic ohmic dissipation (Liu et al., 2008).

There have been two general mechanistic approaches for explaining the observed strong winds on Jupiter and Saturn. The first assumes the dynamics are shallow, such as on a terrestrial planet, and therefore the strong east-west flows can result from 2D geostrophic turbulence (Rhines, 1975, 1979). Several studies have suggested mechanisms for the formation of jets in such systems from either shallow decaying turbulence (e.g., Cho and Polvani, 1996; Scott and Polvani, 2007) or forced turbulence in both barotropic (e.g., Williams, 1978; Showman et al., 2006; Showman, 2007) and baroclinic (e.g., Williams, 1979, 2003; Kaspi and Flierl, 2007) systems. In recent years, a number of terrestrial-type general circulation model (GCM) studies have produced multiple jets that are consistent with the observed flows on all four giant planets (Lian and Showman, 2010; Liu and Schneider, 2010). The alternative approach suggests that the observed jets are the surface manifestation of convective columns originating from the hot interiors of the giant planets (Busse, 1976, 1994). It has been demonstrated in 3D numerical rotating convection models that the interaction of such internal convection can lead to equatorial superrotation and multiple jets caused by convective columns (e.g., Aurnou and Olson, 2001; Christensen, 2002; Wicht et al., 2002; Heimpel et al., 2005; Kaspi et al., 2009; Jones and Kuzanyan, 2009; Gastine et al., 2013; Chan and Mayr, 2013). These two approaches have been in debate for the last 40 years. Hopefully, the upcoming gravity measurements will able to provide insight into the interior dynamics and help resolve this debate.

Therefore, despite advances over the past 40 years in modeling and theory, and detailed spacecraft and telescopic observations, much of the understanding of the dynamics of the giant planets' atmospheres and interiors is limited to the observed outer cloud level. The upcoming gravity measurements by Juno and Cassini provide a new opportunity to probe the dynamics beneath this cloud level and hopefully shed light on the mysteries of the interiors of the giant planets.

1.2. Inferring the depth of the zonal flows from gravity measurements

Earth's atmosphere is less than one millionth of the mass of the solid planet, and therefore any density perturbation associated with the atmospheric dynamics has a very small affect on the planet's gravity field. For example, even the largest air density variations across strong weather fronts on Earth, of order $\sim$ 0.1 kg m^{-3}, will cause gravity variation above them that are at least four orders of magnitude smaller than the effect of Earth's oblateness, which itself has only a 0.3% effect on the mean surface gravity (varying from 9.82 m s^{-2} at the pole to 9.79 m s^{-2} near the equator). However, since the giant gas planets are composed mainly of light elements, and have no solid surface, the relative effect of density perturbations due to internal and atmospheric dynamics can be more significant. Particularly, if the strong winds extend deep enough into the planet's interior, their relative effect on gravity becomes large. This is suggested by Fig. (2), which shows the percentage of the mass involved in the outer layers of the planet as function of the radial distance. For example, if as hypothesized by Liu et al. (2008), only the outer 4% of the radius have significant flows in them, that will already involve 1% of the mass of the planet.

Hubbard (1982) pointed out that if the observed flows on Jupiter correspond to permanent cylindrical structures, then they

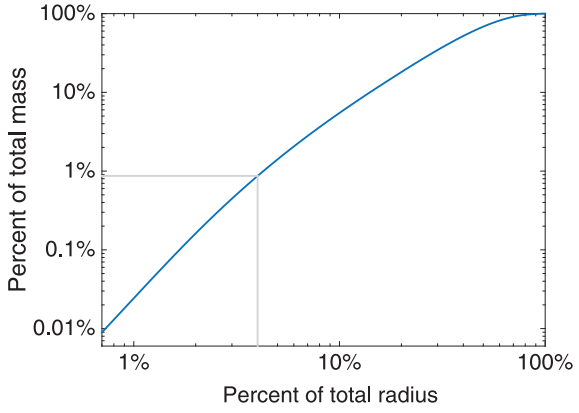

Fig. 2. The mass distribution of Jupiter in terms of the percentage of total mass as function of the percentage of total radius measured from the outside. Based on the internal model of Guillot and Morel (1995).

might give measurable corrections to the gravity field of a rigidly rotating hydrostatic planet. Following this, Hubbard (1999) showed using a potential theory model that such perturbations can be measurable by an orbiting spacecraft, and particularly are likely to give a signal stronger than the solid-body gravity field beyond the 10th gravity moment. This theoretical result was one of the key drivers for the Juno mission. This approach was recently further developed using a more accurate concentric Maclaurin spheroid (CMS) model of the planet's interior (Hubbard, 2012, 2013; Hubbard et al., 2014; Wisdom and Hubbard, 2016).

These studies have allowed accurate estimation of the gravity field, but are limited to cylindrically symmetric, fully barotropic flows (see discussion below). A second approach proposed was using thermal wind balance models (Kaspi, 2013; Kaspi et al., 2010, 2013; Liu et al., 2013, 2014; Zhang et al., 2015), which can calculate the gravity field resulting from any given flow field. However these models have traditionally assumed a spherically symmetric reference state. They are thus unable to calculate the static (solid-body) gravity spectrum, and neglect the effect of the planet's oblateness on the dynamic gravity moments.

A third approach involves using full 3D numerical simulations, and calculating the resulting gravity perturbations by analyzing the density perturbations arising from dynamics (Kaspi et al., 2010; Glatzmaier, 2014). While this approach allows one to consider much more complex flow fields resulting from the dynamics of the GCMs, it only gives specific realizations of the flow, and does not allow for systematic exploration of how the gravity field depends on the dynamics.

In addition, all studies to date have been only in the direction of forward modeling, whereby, given a hypothetical or simulated wind structure, the gravity moments are calculated via the effect of these winds on the density structure (e.g., Hubbard, 1999; Kaspi et al., 2010; Kong et al., 2012; Liu et al., 2013). However, in order to analyze the gravity field that will be detected by Juno and Cassini, an inverse problem needs to be solved, calculating the zonal wind profile given the gravity field (Galanti and Kaspi, 2016). This poses a challenge, since a gravity field is not necessarily invertible and a given gravity field might not have a unique corresponding wind structure. Nonetheless, progress has been made inverting the thermal wind equation (Galanti and Kaspi, 2016).

Given the major differences between these methods, the goal of this study is to develop a unified theoretical framework for the analysis of the gravity data. We discuss the several proposed approaches for relating the dynamics to the density field, focusing on ways to compare the different methods. This is important both for the validation of the models, and for their calibration at the limits where they can be meaningfully compared. A specific difficulty arrises from separating the static and dynamical contributions to gravity, since models that account for the full oblateness of the planet (and thus include the full static contributions), cannot account for complex wind fields. Therefore one of the prime objectives of this study is to investigate the effect of the spherical assumption on the thermal wind model through a systematic comparison to the potential theory and CMS methods in the deep barotropic flow limit where these methods can be compared. The paper is organized as follows: Section 2 discusses the theoretical background for relating the flow field to gravity, specifically in the potential theory, CMS, and thermal wind frameworks. Section 3 shows the analytic equivalence of the potential-theory and thermal-wind methods in the barotropic limit, and discusses different representations of the thermal-wind equation in this barotropic limit. Section 4 discusses how the three models are implemented numerically, and compares results for the dynamically induced gravity harmonics that these methods predict. In Section 5 we discuss the numerical results, and present another comparison between the models when the flow is barotropic, yet limited to the outer regions of the planet. We conclude in Section 6.

2. Theory

For both the Juno and Cassini measurements we are interested in the relation between the gravity field and the large scale flow. To leading order, we can assume that the deviations from the time and zonal mean are small relative to the large scale time-zonal mean flow (Fig. 1). Therefore in the following analysis we do not consider any temporal or zonal variations to the flow. The dynamical induced variations to the gravity field are by definition a small perturbation to the gravity field. Roughly, given the properties of the planet and the amount of angular momentum involved in differential rotation (even for the most extreme cases of full differential rotation penetrating through the planet), the dynamical signal expected, compared to the surface gravity of ~ 25 m s^{-2}, is of the order of several mgal, meaning that it is $O(10^{-6})$ weaker than the surface gravity. Yet, due to the accuracy of the measurements such a signal should be detectable, and similar analysis has been demonstrated in the past in other planetary applications (e.g., Iess et al., 2014).

Relating the gravity and velocity fields can be divided into a two step problem: first calculating the dynamically balanced density field given a wind field, and then integrating this wind-induced density field to calculate the wind-induced gravity anomalies. We begin with discussing the latter, which is straightforward, and in Sections 2.1–2.3 we discuss the methods to do the former, which is non-trivial.

The gravity field is the gradient of the gravitational potential, $\nabla V(\mathbf{r})$. The external gravitational potential at radial coordinate r and colatitude θ can be expanded as

$$V(r,\theta) = \frac{GM}{r}\left(1 - \sum_{n}^{\infty} J_n \left(\frac{a}{r}\right)^n P_n(\cos\theta)\right), \tag{1}$$

where G is the gravitational constant, M is the planetary mass, a is the mean planetary radius and P_n is the nth Legendre polynomial (Hubbard, 1984). Here we have used the standard expansion into zonal gravitational harmonics J_n, and assumed the tesseral field resulting from longitudinal flow variations is identically zero. For both Jupiter and Saturn, to leading order the flow is zonally symmetric (e.g., Choi and Showman, 2011), and therefore this assumption is valid. Nonetheless, depending on the depth of the jets and vortices, it is possible that the tesseral field will be measurable, and if features such as the Great Red Spot are deep enough they may be resolved in the gravity measurements (Parisi et al., 2016). For the purpose of this study, we neglect these longitudinal variations and assume only axisymmetric gravity harmonics. These gravity harmonics are given by

$$J_n = -\frac{2\pi}{Ma^n}\int_{-1}^{1} d\mu \int_{0}^{R(\mu)} r^{n+2} P_n(\mu)\rho(r,\mu)dr, \tag{2}$$

where $\mu = \cos\theta$ and $R(\mu)$ is the radial coordinate of the surface of the planet, and we have trivially integrated over longitudes. Thus, to calculate the gravity harmonics, we must first solve for the density field ρ and also derive the shape of the planet, $R(\mu)$. Note that if the planet's static gravity field is perfectly north-south hemispherically symmetric, the odd static gravity harmonics would be identically zero. However, since the wind structure and therefore the resulting density perturbations are not hemispherically symmetric, we expect non-zero dynamical contributions to the odd gravity harmonics (Kaspi, 2013).

In this paper we compare three methods for solving for the wind-induced density field: the potential theory method (PT) of Hubbard (1999), the concentric Maclaurin spheroid method (CMS) of Hubbard (2013), and the thermal wind balance method (TW)

of Kaspi et al. (2010). Both the PT and CMS methods work in an inertial frame, and introduce dynamics by means of a rotational potential. These two methods model Jupiter as an $n = 1$ polytrope (Hubbard, 1975, 1982; Hubbard et al., 1975), a good approximation to Jupiter's interior. Invoking the Taylor–Proudman theorem (e.g., Pedlosky, 1987), such a barotropic equation of state constrains the flow to be constant along cylinders. Wisdom has developed a further method of solution (1996, unpublished) for the density field of such a differentially rotating $n = 1$ polytrope, which has been found to produce solutions in good agreement with the CMS method (Wisdom and Hubbard, 2016). Our third method, thermal wind balance, differs in several important ways from these barotropic methods, and to date has been discussed independently in the literature. Firstly, TW does not assume any particular equation of state, and can therefore model more realistic wind structures (indeed *any* wind structure) which are baroclinic. Secondly, TW works in a frame rotating with the planet, assuming the Rossby number is small such that geostrophic balance holds. Finally, the thermal wind method has traditionally assumed the dynamics are a perturbation to a spherically symmetric leading order reference state, and so naively neglects the effects of the oblate shape of the planet. However, this is not a necessary feature of thermal wind methods; indeed, a forthcoming paper will derive and investigate a fully oblate generalization of the thermal wind equation (Galanti et al., 2016). In this paper we compare the fully barotropic models (PT and CMS) with the spherical thermal wind equation, and thereby assess the validity of its sphericity assumption.

2.1. Potential theory method

Following Hubbard (1999), the $n = 1$ polytropic equation of state enables us to derive a differential equation for the density field which we then solve numerically. We begin with the familiar Euler equation, assuming steady-state and negligible viscosity. In the inertial frame this takes the form,

$$(\mathbf{v}\cdot\nabla)\mathbf{v} + \frac{1}{\rho}\nabla p + \nabla V = 0, \tag{3}$$

where $\mathbf{v}$ is the velocity field in the inertial frame, p is pressure, ρ is density, and V is the gravitational potential such that the gravitational force per unit volume is $-\rho\nabla V$. The polytrope relation is $p = K\rho^2$, where K is a constant adjusted to fit the radial boundary conditions, and thus $\frac{1}{\rho}(\nabla p) = 2K\nabla\rho$. We take the divergence of Eq. (3), giving

$$\nabla\cdot[(\mathbf{v}\cdot\nabla)\mathbf{v}] + 2K\nabla^2\rho + 4\pi G\rho = 0, \tag{4}$$

where Poisson's equation for the gravitational potential has been used. Defining the wavenumber k in terms of other constants $k^2 = 2\pi G/K$ gives

$$\nabla\cdot[(\mathbf{v}\cdot\nabla)\mathbf{v}] + 2K\nabla^2\rho + 2Kk^2\rho = 0. \tag{5}$$

The barotropic relation requires angular velocity be a function only of distance from the rotation axis, so that $\mathbf{v} = l\Omega(l)\hat{\mathbf{e}}_\phi$, in cylindrical coordinates (l, ϕ, z). We find that the advective term evaluates to $(\mathbf{v}\cdot\nabla)\mathbf{v} = -l\Omega^2\hat{\mathbf{e}}_l$ (which is the centripetal acceleration, consistent with Eq. (3) being the equation of motion), and therefore the divergence of the advective term is then

$$\nabla\cdot[(\mathbf{v}\cdot\nabla)\mathbf{v}] = -2\Omega^2 - 2l\Omega\frac{\partial\Omega}{\partial l}. \tag{6}$$

Hence, taking the divergence of Eq. (3) yields an inhomogeneous Helmholtz equation

$$\nabla^2\rho + k^2\rho = \frac{1}{2K}\left(2\Omega^2 + 2l\Omega\frac{\partial\Omega}{\partial l}\right). \tag{7}$$

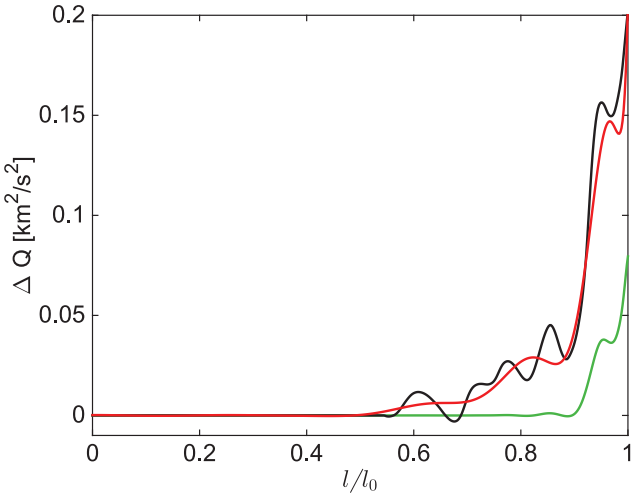

Fig. 3. Perturbation to Jupiter's rotational potential (Eq. 8), where ΔQ is defined in Eq. (11). The black curve is derived from the observed northern hemisphere wind profile (Fig. 1), while the red line shows a polynomial expansion of ΔQ in powers of l/l_0 truncated at 24th order (Eq. 39), where l_0 is the equatorial radius. The truncation is necessary for meaningful high order harmonics (see Section 4). The green line is the solution limited to the outer radius discussed in Section 5.1. (For interpretation of the references to color in this figure legend, the reader is referred to the web version of this article.)

We can express the forcing term on the right hand side in terms of the rotational potential due to zonal flow Q defined by

$$Q(l) = \int_0^l dl' l'\Omega^2(l'). \tag{8}$$

Again working in cylindrical polar coordinates, the gradient of Q (with respect to l) is given by $\nabla Q = l\Omega^2(l)\hat{\mathbf{e}}_l$. Note that $-\nabla Q$ gives the centripetal acceleration, which is why Q is termed the rotational potential. The Laplacian of Q is $\nabla^2 Q = 2\Omega^2 + 2l\Omega\frac{\partial\Omega}{\partial l}$, and thus Eq. (7) can be written in terms of the rotational potential Q

$$\nabla^2\rho + k^2\rho = \frac{1}{2K}\nabla^2 Q, \tag{9}$$

as in Hubbard (1999). The full differential rotation wind structure is contained in the rotational potential term, which is the source of inhomogeneity in this differential equation for ρ. We write $\Omega(l) = \Omega_0 + \delta\Omega(l)$, expanding about a solid body reference state, with $\delta\Omega \ll \Omega_0$. Hence

$$Q(l) = Q_0(l) + \Delta Q(l), \tag{10}$$

where $Q_0(l) = \frac{1}{2}\Omega_0^2 l^2$ and

$$\Delta Q(l) = \int_0^l dl' l' 2\Omega_0\delta\Omega(l') \tag{11}$$

is the dynamically-induced perturbation. Fig. 3 shows the differential potential corresponding to an extension of Jupiter's Northern hemisphere surface winds along cylinders (black). The "truncated" wind structure that is used in Section 4 is also shown (red). We neglect the term second order in $\delta\Omega(l)$.

Following Hubbard (1999), Eq. (9) must be solved with the boundary condition that ρ vanishes on the planet's surface, $R(\mu)$, which is an equipotential. For giant gas planets the definition of this outer surface is somewhat arbitrary since the atmosphere thins continuously out from the center of the planet. For convenience, we define the surface to be the 1 bar isobar. The general solution to Eq. (9) is the sum of a complementary function ρ_C and a particular integral ρ_P. The complementary function ρ_C, which itself solves the homogeneous Helmholtz equation $\nabla^2\rho_C + k^2\rho_C = 0$, is obtained by separation of variables in spherical coordinates and

involves an expansion in Bessel functions,

$$\rho_C = \sum_{n=0,2,\ldots}^{\infty} A_n j_n(kr) P_n(\cos\theta), \tag{12}$$

where j_n is the nth spherical Bessel function of the first kind, P_n is the n$^{\text{th}}$ degree Legendre polynomial, and A_n are coefficients. The particular integral can be written in the form

$$\rho_p(l) = \left(\Omega_0^2/2\pi G\right)(1 + f(l)), \tag{13}$$

and found by numerically integrating Eq. (9). The complete density field is given by $\rho = \rho_p + \rho_C$. The A_n, together with the wavenumber k, must be determined using the boundary condition.

2.2. Concentric Maclaurin spheroid (CMS) method

The CMS method involves discretizing the continuous density field of the first method, and is both simpler and more numerically stable than the PT method. We provide only a schematic introduction to the method, which is mathematically intricate, here. Hubbard (2012) lays the foundation for the CMS method, presenting a numerical method which solves for the equilibrium shape of a rotating *constant density* planet, for which an analytic solution exists in the form of the Maclaurin spheroid. This is achieved by requiring that the sum of the gravitational potential (which we expand in gravity moments as in Eq. (1)) and the rotational potential (10) be constant on the surface of the planet, $R(\mu)$. Because calculating the gravity harmonics itself requires knowledge of $R(\mu)$, this problem is solved by iterating to a self-consistent solution. This method was extended from the constant density Maclaurin spheroid to non-constant density barotropes in Hubbard (2013). The trick is to represent a continuously varying density structure by a discrete set of N layers, in each of which the density is constant. This onion-like structure may be decomposed into a set of N concentric Maclaurin spheroids (hence the name of this method). The exterior gravitational potential is simply the sum of the partial potentials due to each spheroid, by the principle of superposition. We must then self-consistently find the gravity moments such that:

1. The surfaces of *each* of these CMSs are equipotentials, where the potential at each surface receives contributions from both the CMSs interior and exterior to it. Schematically, the total potential is

   $$U \equiv V_{\text{int}} + V_{\text{ext}} + Q, \tag{14}$$

   and this must be constant on each level surface. The rotational potential Q is given exactly as in Eq. (10).
2. The densities of each of these CMSs are fitted to the desired barotrope, in our case the $n = 1$ polytrope $p = K\rho^2$. To see how this can be done, observe that the hydrostatic equation in our non-rotating frame is $\nabla p = \rho \nabla U$. This is integrated within each constant-density layer to get the pressure at the bottom of the jth layer:

   $$P_j = P_{j-1} + \rho_{j-1}\left(U_j - U_{j-1}\right). \tag{15}$$

Note that the CMS method can model *any* desired barotropic relation, whereas the PT method of solution using spherical Bessel functions only works for the $n = 1$ polytropic equation of state, from which follows the Helmholtz Eq. (9). The analytic development of the CMS method is lengthy, for which we refer the reader to Hubbard (2013).

2.3. Thermal wind (TW) method

To derive the thermal wind method (Kaspi et al., 2009, 2010), our starting point is the Euler equation in a reference frame rotating with the planet (System III rotation vector (May et al., 1979; Riddle and Warwick, 1976) with $\Omega_0 = 1.75 \times 10^{-4}$ corresponding to a period of 9.92 hours). Consequently, there are two additional terms to Eq. 3 corresponding to the Coriolis and the centrifugal forces[1]:

$$(\mathbf{u}\cdot\nabla)\mathbf{u} + 2\Omega_0 \times \mathbf{u} + \Omega_0 \times (\Omega_0 \times \mathbf{r}) = -\frac{1}{\rho}\nabla p - \nabla V. \tag{16}$$

As the giant planets are rapid rotators and characterized by large scale flow, the Rossby number, which is the ratio of the inertial accelerations to the Coriolis accelerations, is small. We thus work in the limit of small Rossby number, which is similar (but not identical) to the assumption that $\delta\Omega \ll \Omega$ in the potential theory model (Section 4.1). In this approximation, the fluid is in geostrophic balance (Pedlosky, 1987), that is, the advective term in Eq. (16) is an order Rossby number smaller than the Coriolis term so that we can neglect the advective term:

$$2\Omega_0 \times \mathbf{u} = -\frac{1}{\rho}\nabla p + \mathbf{g}^*, \tag{17}$$

where $\mathbf{g}^*$ is the effective gravitational field, $\mathbf{g}^* = -\nabla V + l\Omega_0^2\hat{\mathbf{e}}_l$, where the second term is the centrifugal acceleration. Multiplying Eq. (17) by the density ρ, and taking the curl gives

$$2\nabla \times (\Omega_0 \times \rho\mathbf{u}) = \nabla \times (\rho\mathbf{g}^*), \tag{18}$$

where $\mathbf{g}^*$ is the effective gravitational field, $\mathbf{g}^* = -\nabla\phi$, which includes the effects of the centrifugal acceleration. Expanding both sides of this equation gives:

$$2\{\rho\mathbf{u}(\nabla\cdot\Omega_0) - \Omega_0(\nabla\cdot\rho\mathbf{u}) + (\Omega_0\cdot\nabla)\rho\mathbf{u} - (\rho\mathbf{u}\cdot\nabla)\Omega_0\} = -\rho\nabla\times\mathbf{g}^* - \nabla\rho\times\mathbf{g}^*. \tag{19}$$

Noting that Ω_0 is a constant vector, that the steady state continuity equation $\nabla\cdot(\rho\mathbf{u}) = 0$ holds and that $\nabla\times\mathbf{g}^* = \nabla\times\nabla\phi = 0$, we deduce the equation:

$$2\Omega_0\cdot\nabla(\rho\mathbf{u}) = -\nabla\rho\times\mathbf{g}^*. \tag{20}$$

This thermal wind relation (Kaspi et al., 2009) is different to the standard thermal-wind used in atmospheric science for a shallow atmosphere, in that the derivatives on the left hand side are in the direction of the spin axis and not in the radial direction (an approximation which holds when the planetary aspect ratio is small), and the right hand side involves the full density and effective gravity. Thus, this is a general expression applicable for a rotating atmosphere at any depth as long as the Rossby number is small[2].

A simplification to this equation that was taken for example in Kaspi et al. (2010), and will be further evaluated in this paper, is to assume spherical geometry. The advantage of this approach, as will be shown below, is that the dynamically induced gravity harmonics can be easily and uniquely determined. We define a spherically symmetric reference state, characterized by pressure $\tilde{p}(r)$ and density $\tilde{\rho}(r)$, that is in hydrostatic balance:

$$\nabla\tilde{p}(r) = \tilde{\rho}(r)\mathbf{g}(r), \tag{21}$$

where the mean gravity $\mathbf{g}(r)$ is that due to the hydrostatic reference density $\tilde{\rho}(r)$. Primes (ρ', p') are used to denote spatial fluctuations from this basic state due to dynamics, such that the density and pressure are given by

$$\rho = \tilde{\rho}(r) + \rho'(r,\theta), \tag{22}$$

$$p = \tilde{p}(r) + p'(r,\theta), \tag{23}$$

[1] To avoid confusion we denote differently the wind vector in the inertial frame ($\mathbf{v}$) in Section 2.1 and in the rotating frame ($\mathbf{u}$) in Section 2.3.

[2] Note that for consistency with the definition of the sign of gravity in Hubbard, 1999 (Section 2.1 here), there is a sign difference in Eq. (20) when compared with Kaspi et al., 2009.

where the fluctuations are assumed to be small perturbations to the basic state ($\widetilde{\rho} \gg \rho'$, $\widetilde{p} \gg p'$). Under the assumption of azimuthal symmetry, and since we are interested only in the long-term time averaged fluctuations, temporal and longitudinal fluctuations have been neglected in the primed parameters. To simplify our analysis, we assume that the gravitational acceleration appearing in Eq. (20) is simply that due to the hydrostatic reference density $\mathbf{g}(r)$; we neglect both the centrifugal acceleration (hence enforcing sphericity) and the perturbation $\mathbf{g}'(r, \theta)$ that arises due to the density anomaly ρ', which includes a non-radial component. Zhang et al. (2015) include this perturbation $\mathbf{g}'(r, \theta)$ to derive the thermal gravitational wind equation (TGWE), which is much more difficult to solve. They show that the results for the gravity harmonics can deviate by up to a factor of 2 (for the most extreme cases) from the thermal wind model described here if such a non-radial component of $\mathbf{g}$ is retained. In a forthcoming paper, we will show that this additional term is but one of several more terms all of sub-leading magnitude to the spherically symmetric term which we here retain – all (or none of) these subleading terms must be included for a consistent application of perturbation theory (Galanti et al., 2016).

We proceed with our simpler incarnation of the thermal wind model. Since $\widetilde{\rho}$ is a function of the radial coordinate only, and $\mathbf{g}(r)$ is purely radial, we have $\nabla\widetilde{\rho} \times \mathbf{g} = 0$. Given also that $\widetilde{\rho} \gg \rho'$, Eq. (20) becomes

$$2\Omega_0 \cdot \nabla(\widetilde{\rho}\mathbf{u}) = -\nabla\rho' \times \mathbf{g}, \tag{24}$$

which allows one to determine the density anomaly ρ', given both a suitable model for the dynamics **u,** and an internal hydrostatic density profile $\widetilde{\rho}$ (Kaspi et al., 2010). This density anomaly then perturbs Jupiter's gravity field, producing contributions to the gravity harmonics associated with the dynamics only:

$$\Delta J_n = -\frac{2\pi}{Ma^n}\int_{-1}^{1} d\mu \int_0^{R(\mu)} r^{n+2} P_n(\mu)\rho'(r,\mu)dr. \tag{25}$$

Integrating Eq. (24) to find ρ' (for use in (25)) is discussed in Section 4.3, but from the form of (24) it is obvious that ρ' can only be determined up to an unknown function of radius r assuming spherical symmetry. However such a function will not project onto the gravity harmonics when multiplied by the P_n in (25), since the P_n have zero mean. Therefore in spherical geometry the dynamical gravity anomalies can be uniquely determined, despite the density anomaly being determined only up to an unknown constant of integration. This is further discussed in Section 4.3.

3. Model equivalence in the barotropic limit

In this section, we demonstrate the equivalence of the thermal-wind relation to the Helmholtz Eq. (7), in the limiting barotropic case of full differential rotation. We also demonstrate the equivalence of different forms of thermal-wind balance that often appear in the literature. Readers interested in the numerical comparison between the methods presented in Section 2 can skip to Section 4.

3.1. The equivalence of the potential-theory and thermal-wind models in the barotropic limit

The thermal wind and Helmholtz equations can of course only be equivalent if describing the same physics, and this encompasses both the wind structure and also the shape of the planet. Therefore we must model full differential rotation, and consider the thermal-wind equation prior to making the sphericity assumption, that is, in the form (20). While in this study we have then enforced sphericity, this is not essential for implementing the thermal wind method. Hence demonstrating the equivalence of this generalized thermal wind equation to the Helmholtz equation of potential theory is an important step in bringing together these two frameworks of analysis.

Eq. (16), together with the single assumption of small Rossby number, fully implies the general thermal wind relation (20). Thus, demonstrating the equivalence of Eq. (16) to the Helmholtz relation (7) is sufficient to demonstrate the analytic equivalence of these two methods. These equations are related simply by a change of reference frames, which we now show explicitly. We begin with the momentum Eq. (16), and input our differential rotation wind structure, $\mathbf{u} = l(\Omega(l) - \Omega_0)\hat{\mathbf{e}}_\phi$ (noting that **u** is the velocity with respect to the rotating frame). Eq. (16) is then

$$-l(\Omega-\Omega_0)^2\hat{\mathbf{e}}_l - 2l\Omega_0(\Omega-\Omega_0)\hat{\mathbf{e}}_l - l\Omega_0^2\hat{\mathbf{e}}_l = -\frac{1}{\rho}\nabla p - \nabla V. \tag{26}$$

We now take its divergence. As in the inertial frame case above, the divergence of the pressure gradient and gravitational terms is $\nabla\cdot\left(\frac{1}{\rho}\nabla P + \nabla V\right) = 2K(\nabla^2\rho + k^2\rho)$, when using a polytropic relation of index unity. Taking the divergence of the terms on the left hand side $\left(\frac{1}{l}\frac{\partial}{\partial l}\right)$ then yields

$$2K(\nabla^2\rho + k^2\rho) = 2(\Omega-\Omega_0)^2 + 2l(\Omega-\Omega_0)\frac{\partial\Omega}{\partial l} + 2\Omega_0\left(2(\Omega-\Omega_0) + l\frac{\partial\Omega}{\partial l}\right) + 2\Omega_0^2. \tag{27}$$

That gives

$$\nabla^2\rho + k^2\rho = \frac{1}{2K}\left(2\Omega^2 + 2l\Omega\frac{\partial\Omega}{\partial l}\right), \tag{28}$$

which is identical to Eq. (7), derived in the inertial reference frame. The question then is, how far does the sphericity assumption drive us away from this equivalence? In Section 4.3 we evaluate quantitatively the errors introduced by this sphericity assumption by comparing the results of the PT and CMS methods to the TW method.

3.2. Thermal wind balance in the barotropic limit

The previous section showed the equivalence of the PT and TW methods in the barotropic limit. It is important to note that the barotropic limit is *not* when the right hand side of Eq. (24) vanishes (there has been confusion about this in the literature), in which case Eq. (24) would imply that $\widetilde{\rho}\mathbf{u}$ is constant along the direction of the spin axis. Rather, the barotropic limit (by definition $\nabla p \| \nabla\rho$), or equivalently the Taylor–Proudman theorem (Taylor, 1923), implies that the velocity itself (not multiplied by $\widetilde{\rho}$) is constant along the direction of the spin axis. This can be easily seen by taking the curl of Eq. (16), which in the limit of small Rossby number gives (Pedlosky, 1987),

$$(2\Omega\cdot\nabla)\mathbf{u} - 2\Omega\nabla\cdot\mathbf{u} = -\frac{\nabla\rho\times\nabla p}{\rho^2}. \tag{29}$$

In the barotropic limit, where by definition $\nabla\rho\times\nabla p = 0$, the azimuthal component of this equation implies

$$\left(2\Omega\hat{z}\right)\frac{\partial u}{\partial z} = 0, \tag{30}$$

meaning that the zonal flow does not change along the direction of the spin axis ($\hat{z}$), where u is the azimuthal wind component. If in addition, the fluid is Boussinesq ($\nabla\cdot\mathbf{u} = 0$) also the full velocity vector is constant along the direction of the spin axis. This is what is behind the assumption that the flow velocity along cylinders will remain constant in the limit of a purely barotropic fluid (e.g., Busse, 1976; Hubbard, 1999).

The purpose of this section is to clarify that in the barotropic limit the thermal wind equation written as in Eq. (24) reduces to the Taylor-Proudman theorem. The reason the right hand side of

Eq. (24) does not vanish in the barotropic limit is that the term $\nabla\rho' \times \mathbf{g}$ is not a purely baroclinic term, as the gravity is related only to the static component of the density through the hydrostatic relation where $\nabla\tilde{p} = \tilde{\rho}\mathbf{g}$. Beginning from Eq. (24) and using the hydrostatic relation gives

$$2\Omega \cdot \nabla(\tilde{\rho}\mathbf{u}) = -\frac{1}{\tilde{\rho}}\nabla\rho' \times \nabla\tilde{p}. \tag{31}$$

We can expand the full baroclinic term, $\nabla\rho \times \nabla p$, as

$$\nabla\rho \times \nabla p = \nabla\tilde{\rho} \times \nabla p' + \nabla\rho' \times \nabla\tilde{p}, \tag{32}$$

where in (32) the term $\nabla\tilde{\rho} \times \nabla\tilde{p}$ vanished because $\nabla\tilde{\rho} \parallel \nabla\tilde{p}$, and $\nabla\rho' \times \nabla p'$ is a higher order term and therefore can be neglected. Then Eq. (31) can be rewritten as

$$2\Omega \cdot \nabla(\tilde{\rho}\mathbf{u}) = -\frac{1}{\tilde{\rho}}\left(\nabla\rho \times \nabla p - \nabla\tilde{\rho} \times \nabla p'\right). \tag{33}$$

Using the assumption of small Rossby number and therefore that to leading order the flow is geostrophic (Eq. 17), i.e., $\nabla p' = -\tilde{\rho}(2\Omega \times \mathbf{u}) + \rho'\mathbf{g}$ (after subtracting the mean state hydrostatic term) Eq. (33) gives,

$$2\Omega \cdot \nabla(\tilde{\rho}\mathbf{u}) = -\frac{\nabla\rho \times \nabla p}{\tilde{\rho}} - \nabla\tilde{\rho} \times \left(2\Omega \times \mathbf{u} - \frac{\rho'}{\tilde{\rho}^2}\nabla\tilde{p}\right). \tag{34}$$

The vector triple product in Eq. (34) can be expanded as

$$\nabla\tilde{\rho} \times 2\Omega \times \mathbf{u} = 2\Omega(\nabla\tilde{\rho} \cdot \mathbf{u}) - \mathbf{u}(\nabla\tilde{\rho} \cdot 2\Omega), \tag{35}$$

which can be plugged into Eq. 34, and expanding also the left hand side of Eq. 34 gives

$$2\Omega\tilde{\rho} \cdot \nabla\mathbf{u} = -\frac{\nabla\rho \times \nabla p}{\tilde{\rho}} - 2\Omega(\nabla\tilde{\rho} \cdot \mathbf{u}), \tag{36}$$

where note the second term in (35) and part of the left hand side in Eq. (34) cancel each other. The anelastic approximation, $\nabla \cdot (\tilde{\rho}\mathbf{u}) = 0$, (Durran, 1989), implies that we can rewrite the second term on the right hand side of Eq. 36,

$$2\Omega(\nabla\tilde{\rho} \cdot \mathbf{u}) = -2\Omega\tilde{\rho}(\nabla \cdot \mathbf{u}) \tag{37}$$

so that Eq. (36) becomes

$$2\Omega\tilde{\rho} \cdot \nabla\mathbf{u} - 2\Omega\tilde{\rho}(\nabla \cdot \mathbf{u}) = -\frac{\nabla\rho \times \nabla p}{\tilde{\rho}}. \tag{38}$$

Then, in the purely barotropic limit ($\nabla\rho \times \nabla p = 0$) we retrieve the Taylor–Proudman theorem (Eq. 29). Thus the form (24) is completely consistent with the Taylor–Proudman theorem in the barotropic limit, and in that limit the zonal velocity will be constant along the direction of the spin axis. However, even systems dominated by convection (as might be the interiors of the giant planets) do not need to be purely barotropic, and the right hand side of Eq. (24) can be non-zero resulting in baroclinic shear along the direction of the spin axis. The thermal wind equation can model such baroclinic flows, whereas the PT and CMS methods cannot.

4. Numerical modeling and results

We now implement these three independent methods to calculate the gravity moments for a particular wind structure which we here describe. Since the PT and CMS methods require a barotropic equation of state, we must model a planet rotating on cylinders. This must be north-south hemispherically symmetric, and therefore we perform the analysis using both Jupiter's northern hemisphere (NH) and southern hemisphere (SH) wind profiles separately, as in Hubbard (1999). This results in the odd gravity harmonics being identically zero. Wind profiles are derived from the Cassini flyby surface wind-speed data (Porco et al., 2003), which is more precise and over a wider latitude range than that of Voyager used in Hubbard (1999). However, simply extending the exact surface wind profile along cylinders in fact produces instabilities in the calculation of the higher order gravity harmonics. We use a simplified ("truncated") wind profile that is necessary if the gravity expansion is to converge.

Introduction of the audit-point method for CMS calculations (Hubbard, 2012, 2013; Hubbard et al., 2014) allows us to apply a new convergence test to the results for the $n = 1$ polytrope. Assume that $\Delta Q(l/l_0)$ can be approximated by a polynomial expansion:

$$\Delta Q \approx \sum_{n=0}^{n_{\max}} B_{2n}(l/l_0)^{2n}. \tag{39}$$

Numerical experiments show us that if $n_{\max}$ exceeds about 12 (corresponding to a 24th order polynomial), the maximum error in the surface potential, as calculated using audit points, becomes comparable to the corresponding absolute value of ΔJ_{30}. This means that these high-order terms are dominated by numerical noise (for example they will be vulnerable to sign alternations). It is possible to keep the numerical noise within acceptable limits by choosing $n_{\max} \approx 12$. As is evident in Fig. 3, this procedure smooths out some of the detailed oscillations in the wind profile, but is necessary in order to get meaningful values at high harmonics. That is, the value of $n_{\max}$ at which we truncate represents a trade-off between fidelity to the exact ΔQ and the need for our solutions to converge.

This truncation alters the gravity spectrum, as can be seen in Fig. 4, which shows the gravity harmonics calculated using the potential-theory method (discussed below in 4.1) with and without the truncation. Shown are the dynamical gravity harmonics (ΔJ_n), calculated as the difference between the full solution and the solid-body harmonics (i.e., those calculated with no wind profile). It is evident that the truncation significantly decreases the signal beyond the 24th moment (it also effects to a lesser extent the low-order harmonics). How should we interpret this? Beyond the 24th moment the solid-body contribution is negligible and ΔQ has been truncated, so there should be no contribution to the gravity moments other than nonlinear effects that carry from lower harmonics. Thus the values consistently decrease beyond the truncation level. However the values of these harmonics are not physically meaningful. We use this truncated ΔQ in our PT and CMS calculations. For the TW calculation, we reconstruct a wind-profile $u(r, \theta)$ by differentiating this truncated ΔQ, in order to make consistent comparisons with the PT and CMS results.

4.1. Potential Theory method

Recall from Section 2.1 that the complete density field is given by

$$\rho = \rho_p + \sum_{n=0,2,\ldots}^{\infty} A_n j_n(kr) P_n(\cos\theta). \tag{40}$$

We obtain the particular integral ρ_P directly from the rotational potential ΔQ by Runge–Kutta integration of Eq. (9), and we find $f(l) \ll 1$ because $\delta\Omega \ll \Omega_0$. The complete solution must then be obtained iteratively, since there is a circular chain of dependence between the surface $R(\mu)$, the density coefficients A_n, and the gravity harmonics J_n which we are ultimately trying to find. In words: (i) the boundary condition $\rho|_{r=R(\mu)} = 0$ is used to fix the coefficients A_n and the wavenumber k; (ii) this boundary surface $R(\mu)$ is determined by the condition that the surface is an equipotential; i.e., that $V + Q = \text{const}$ (iii) the gravitational potential V is an expansion in the gravitational moments J_n, which require knowledge of both $\rho(\mathbf{r})$ (that is, the coefficients A_n) and $R(\mu)$. We must suppose

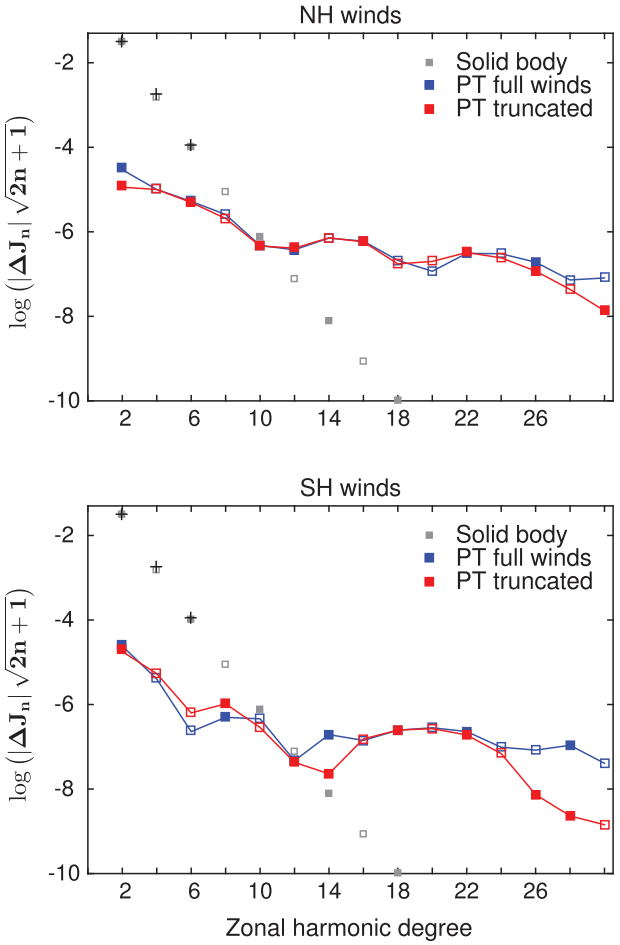

Fig. 4. A comparison between the zonal gravity harmonics (ΔJ_n) as calculated from the potential-theory model using NH (top) and SH (bottom) winds for cases of the full (blue) and truncated winds (red). The solid-body solution as calculated by the potential-theory model with no dynamics appears in gray. Full (open) markers denote positive (negative) values on this log scale. Plus signs mark the observed values for Jupiter. (For interpretation of the references to color in this figure legend, the reader is referred to the web version of this article.)

an initial trial solution and iterate until convergence is achieved. Hubbard (1975) has derived, for the solid-body case, leading order expansions of J_2, J_4, J_6, A_0, A_2, A_4 and k in the small rotation parameter $q = \Omega_0^2 a^3/GM < 0.1$, which constitute a suitable such trial solution. We then iterate the following sequence of calculations until convergence is achieved:

- Recalculate the even gravity harmonics J_n using Eq. (2) up to our cut-off $n = 24$. Perform the integrals by Gaussian quadrature with $2n = 48$ quadrature points, which should yield the exact values of these integrals to within the floating point precision of the computer (Hubbard, 2012, 2013).
- Recalculate the level surface $R(\mu)$ for this modified gravitational potential $V(\{J_n\})$, by minimizing $(V + Q)|_{R(\mu)} - (V + Q)|_{\text{equator}}$.
- Enforce the boundary condition $\rho_{R(\mu)} = 0$ with this modified shape, by refitting the wavelength k and the density coefficients A_n using a Legendre fitting routine.

The results of these PT calculations are plotted in Fig. 4. The final root-mean-square magnitude of the density evaluated on the surface $R(\mu)$ may be used to quantify the degree of convergence of the PT solutions. We find this value to be a fraction $\sim 10^{-6}$ of the mean planetary density.

4.2. CMS method

As introduced in Section 2.2, the CMS method is implemented using a similar iterative scheme to that employed by the PT calculation. As for any such iterative scheme, we must choose an appropriate initial state to iterate from. For the CMS method, this means we need a starting configuration of shapes for our N CMSs (which we can characterize by their equatorial radii, a_i), and the incremental densities of those N CMSs $\delta\rho_i = \rho_i - \rho_{i-1}$, where $i = 0, 1, \ldots, N-1$. We choose our starting values to reproduce the (discretized) density distribution of a non-rotating $n = 1$ polytrope, which is the spherically symmetric distribution

$$\rho(r) = \rho_c \frac{\sin(\pi r/a)}{(\pi r/a)}, \tag{41}$$

as a function of radial distance r from the center of the planet, where ρ_c is the central density, and a is the planet's radius. We use $N = 512$ CMSs, which is a trade-off between a small discretization error, and keeping the computation time (which increases as N^2) manageable (Wisdom and Hubbard, 2016). We then iterate the following sequence of calculations (Hubbard, 2013) until convergence is achieved:

- Recalculate the even gravity harmonics J_n, again by Gaussian quadrature with $2n = 48$ quadrature points.
- Recalculate the fields U and p for the current configuration of CMSs using Eqs. (14) (which uses the current values of the J_n) and (15), respectively.
- Recalculate the level surfaces of our N CMSs by requiring they be surfaces of constant U.
- Calculate the desired densities of each layer by fitting to the required barotrope $p = p(\rho)$ using

$$\rho_j = \rho\left(\frac{1}{2}\left(p_{j+1} + p_j\right)\right), \tag{42}$$

with $\rho(p)$ being the inverse of the barotrope relation. The densities must also be normalized to the correct total mass of Jupiter.

In this study we take the CMS method to provide our most trustworthy benchmark for calculating the gravity moments of a differentially rotating barotrope. Firstly, this is because the CMS method has been shown to be in strong agreement with the independent method of Wisdom (Wisdom and Hubbard, 2016) for a number of test cases. Secondly, the degree of convergence of the CMS solutions has been quantified by applying the audit-point procedure (Hubbard et al., 2014) to each concentric spheroid, and found to be $\sim 10^{-10}$, or four orders of magnitude better than the convergence of the PT calculation. This is most likely due to the numerical imprecision in adjusting the A_n to fix the zero-density surface condition in the PT method, which is sidestepped in the CMS method. Thus, in addition to using the CMS values as our benchmark for assessing the errors introduced by the sphericity assumption of the TW method (which is a principal aim of this paper), we are also in a position to revaluate the accuracy of the PT method of Hubbard (1999).

4.3. Thermal-wind method

In the spherical limit, the thermal wind model is simplified significantly. The azimuthal component of Eq. (24) is

$$2\Omega_0 \frac{\partial}{\partial z}(\tilde{\rho}u) = -\frac{g}{r}\frac{\partial \rho'}{\partial \theta}, \tag{43}$$

where z is used for compactness denoting the direction of the axis of rotation; in spherical coordinates

$$\frac{\partial}{\partial z} = \cos\theta \frac{\partial}{\partial r} - \sin\theta \frac{1}{r}\frac{\partial}{\partial \theta}. \tag{44}$$

Table 1
Comparison of the Jupiter ΔJ_n from the PT, CMS and TW models. Values correspond to those appearing in Fig. 5.

Jupiter dynamically induced gravity harmonics $\times 10^{-6}$	Northern Hemisphere			Southern Hemisphere		
	PT	CMS	TW	PT	CMS	TW
ΔJ_2	12.753	14.319	17.600	20.019	36.653	27.787
ΔJ_4	−10.629	−11.253	−8.179	−5.688	−9.822	−6.071
ΔJ_6	5.160	5.171	3.360	−0.658	−1.354	−2.426
ΔJ_8	−2.126	−2.319	−1.555	1.069	1.584	1.490
ΔJ_{10}	0.473	0.744	0.488	−0.292	−0.212	0.153
ΔJ_{12}	0.418	0.186	0.214	0.043	0.026	−0.046
ΔJ_{14}	−0.732	−0.594	−0.503	0.023	−0.072	−0.163
ΔJ_{16}	0.588	0.611	0.561	−0.155	−0.105	−0.128
ΔJ_{18}	−0.176	−0.290	−0.279	0.251	0.176	0.114
ΔJ_{20}	−0.201	−0.115	−0.163	−0.271	−0.227	−0.175
ΔJ_{22}	0.328	0.291	0.321	0.192	0.205	0.239
ΔJ_{24}	−0.244	−0.232	−0.195	−0.069	−0.065	0.012

To be consistent with the PT and CMS solutions the basic state density profile $\tilde{\rho}$ was set to be that of a non-rotating $n = 1$ polytrope, as given by Eq. (41). Eq. 43 was then integrated over latitude to obtain the density anomaly $\rho'(r, \theta)$ for the zonal wind distribution $u(r, \theta)$ described above,

$$\rho'(r,\theta) = -\int^{\theta} \frac{2\Omega_0 r}{g}\frac{\partial}{\partial z}\left(\tilde{\rho}u\left(r,\theta'\right)\right)d\theta' + \rho_0'(r). \tag{45}$$

Note that the result is determined only up to an integration constant $\rho_0'(r)$, which is a function only of the radial coordinate because the integration is along spherical paths. However, such a function with no angular dependence does not influence the dynamical gravity harmonics ΔJ_n, as in Eq. (25), since for each moment we multiply through by a Legendre polynomial (which are mean-zero) and integrate over all angles. Thus, the gravity perturbation ΔJ_n is fully and uniquely determined by the TW model in the spherical limit. This is only the case when the thermal wind equation is integrated along paths of constant radius r. The simplicity of this method in the spherical limit allows us to perform the integration (45) at very high resolution in only a short computation time. The comparisons undertaken here attempt to assess the validity of making this sphericity assumption, by exploiting the fact that in the barotropic limit of rotation on cylinders there exist complete methods such as the CMS method for calculating the gravity spectrum precisely. Thus, the deviations between the spherical TW and the CMS gravity harmonics give us a measure of the errors introduced by making the sphericity assumption.

5. Discussion

Fig. 5 shows the results for ΔJ_n from the spherical TW model compared to those of the fully oblate PT and CMS models (where for the latter models, which calculate the full gravity harmonics, the ΔJ_n are calculated as the difference between the full and solid-body solutions). Due to the truncation of ΔQ, all three solutions decay beyond the 24th degree – however recall these harmonics are not physically meaningful.

The results show very strong agreement between all three methods for the wind profile derived from northern hemisphere surface winds. For the lower degree harmonics (between ΔJ_2 and ΔJ_8), the PT and CMS agree very closely, with the TW differing by factors $\lesssim 1.5$ (see Table 1 for the numerical values of each solution). This behavior might be expected, because the oblateness, which the TW neglects, will have strongest projections onto these low order harmonics. However for the higher degree harmonics, the TW solutions are in fact closer to the CMS than the PT are (Table 1). This suggests that, for the all-important higher order harmonics for which the effects of the dynamics may actually be measurable over the solid-body contributions, the sphericity assumption does not introduce significant errors into the TW calculation.

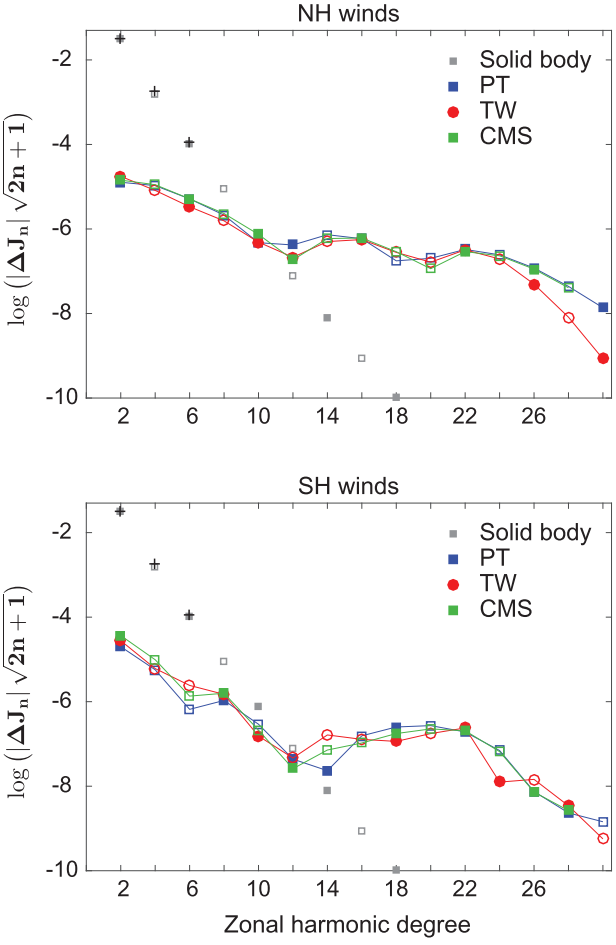

Fig. 5. The zonal gravity harmonics (ΔJ_n) as calculated from the thermal-wind model (red), potential-theory model (blue), and CMS model (green), using NH (top) and SH (bottom) wind profiles. For proper comparison between the models we use the truncated profiles in all cases. The solid-body solution as calculated by the potential-theory model with no dynamics appears in gray. Full (open) markers denote positive (negative) values on this log scale. Plus signs mark the observed values for Jupiter (Jacobson, 2003). (For interpretation of the references to color in this figure legend, the reader is referred to the web version of this article.)

However, for the equivalent southern hemisphere wind profile, there appears to be substantial discrepancies between the results

of all three methods. There are sign alternations at ΔJ_{10}, ΔJ_{12}, ΔJ_{14} and ΔJ_{24}. Crucially, these four harmonics have particularly low magnitudes approaching the noise level (defined by the amplitude of the harmonics beyond the truncation degree). These harmonics are therefore vulnerable to sign changes due to numerical noise. Note that similarly low magnitude harmonics did not arise in the northern hemisphere profile, which was therefore more robust to numerical noise. Moreover, the fact that the PT and CMS predictions themselves disagree significantly at these harmonics suggests that the discrepancies between TW and CMS are not attributable to the TW's sphericity assumption (since both PT and CMS models a fully oblate solutions). Rather, these harmonics are at low enough magnitudes that the numerical precision of all three methods deteriorates significantly.

On balance, these results suggest the sphericity assumption does not significantly degrade the TW results in the barotropic limit of full differential rotation. The TW method has the considerable advantage of being able to input any hypothetical zonal wind distribution including baroclinic cases with wind shear, and so may be extended to model more realistic wind structures whereas the PT or CMS approaches may not. Generally the stronger the shear, the less mass is involved with the flows and the dynamically induced gravity harmonics become smaller (e.g., Kaspi et al., 2010; Kaspi, 2013). It should be noted however that as the magnitude of the gravity harmonics depends on the projection of a specific wind profile on the spherical harmonics, the decay of amplitude with shear is not necessarily linear or monotonic. The TW method possesses several other advantages that derive from its simplicity – most notably its invertibility (Galanti and Kaspi, 2016).

5.1. Barotropic wind limited to the outer radius

As a consequence of pressure ionization, at depths of ~0.9 and ~0.85 the planetary radius the fluid on Jupiter and Saturn, respectively, becomes ionized (Guillot, 2005). It is uncertain how this affects the flow, but it has been suggested that Ohmic dissipation might damp the flow and lead to a quiescent interior (Liu, 2006; Liu et al., 2008). Independently, numerical 3D models of the planet interiors indicate a possible decay in the fluid velocity at depth due to the compressibility of the fluid (Kaspi et al., 2009). This led to studies using the TW approach for estimating the gravity signature since it allows using baroclinic flows. However, because a principal purpose of this study is to assess the validity of the TW method by comparing it against the barotropic potential-surface models, we do not consider baroclinic flows here. Nonetheless, as suggested by Cao and Stevenson (2015), another possible comparison is for barotropic flows in which the dynamics are limited to the outer regions of the planet. This, with the barotropic assumption, implies then the flows will be limited to the equatorial region (meaning damped towards the spin axis). Therefore, in this section we compare the three models for flows limited to the outer radius, with a ΔQ as shown by the green line of Fig. 3, which is similar to the flow considered in Cao and Stevenson (2015). This specific profile is a damped version of the NH wind profile so that there is effectively no flow inside $0.8a$. The wind is weaker than 2.5 m s^{-1} inside $0.9a$ and weaker than 1 mm s^{-1} inside $0.8a$.

The gravity spectra predicted by our three methods for this wind structure are plotted in Fig. 6. All high order gravity harmonics which are measurable above the solid body contribution, that is from ΔJ_{14} upwards, are in excellent agreement between all three methods. This indicates that the impact of oblateness on the high order dynamical moments is not enhanced when the flows are limited to more realistic shallower cases. We therefore expect that also in baroclinic cases (as studied for example in Kaspi et al. 2010), which may be similarly limited in depth, oblateness will have a small effect on the dynamical gravity harmonics. There are,

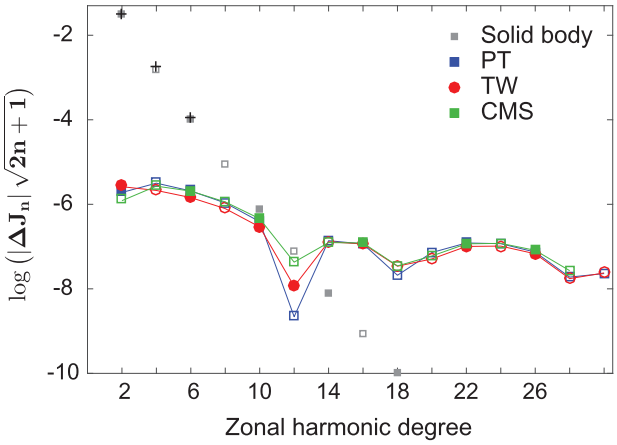

Fig. 6. The zonal gravity harmonics (ΔJ_n) as calculated from the thermal-wind model (red), potential-theory model (blue), and CMS method (green), using the wind profiles limited to the outer 90% of Jupiter's radius. The solid-body solution as calculated by the potential-theory model with no dynamics appears in gray. Full (open) markers denote positive (negative) values on this log scale. Plus signs mark the observed values for Jupiter (Jacobson, 2003). (For interpretation of the references to color in this figure legend, the reader is referred to the web version of this article.)

however, discrepancies at ΔJ_2 (a sign alteration in the CMS calculation) and ΔJ_{12} (differences in sign and order of magnitude between all three methods). Similar to the southern hemisphere profile discussed above, our interpretation is that these discrepancies are a consequence of numerical noise, not the sphericity assumption of the TW. ΔJ_{12} has an extremely small value, below the noise level, and so its value is predominantly an artifact of numerical imprecision in all three methods and is not therefore physical. Note this is consistent with the Euler equation solution of Cao and Stevenson (2015), which also showed a particular drop in magnitude for J_{12}. Similarly, inspecting ΔJ_2, we note that the dynamical contribution is a large factor of order 10^5 times smaller than the solid body contribution (this factor is far greater than for the two wind profiles considered in Fig. 5). Audit-point methods suggest a significantly larger noise level for the CMS calculation with this wind profile than those modeled in Fig. 5, because it is essentially untruncated. These errors thus leave the residual ΔJ_2 vulnerable to a sign alteration once we have subtracted the solid body contribution. Furthermore, the fact that the sign is different for the CMS method, while the TW and PT agree, suggests there is no evidence that it is the sphericity assumption of the TW that is responsible for this sign discrepancy. From the analysis of the three different wind profiles used in our modeling, a general picture emerges: discrepancies between the three models emerge only when the signal to noise ratio is low, with minimal evidence that the TW is less reliable than the fully oblate potential-surface methods.

6. Conclusion

In anticipation of the upcoming Juno and Cassini gravity experiments in 2016–2018 several studies over the last few years have attempted to provide predictions for the high-order gravity field based on theoretical surface and internal flow profiles. This has been done using either strictly barotropic models (e.g., Hubbard, 1999; Kong et al., 2012; Wisdom and Hubbard, 2016), or thermal-wind type models (e.g., Kaspi et al., 2010; Kaspi, 2013; Liu et al., 2013; Zhang et al., 2015). The purpose of this study is to provide a comparative analysis of these two distinct approaches from both theoretical and numerical perspectives, with a quantitative comparison of the predicted gravity moments. We include two independent barotropic methods in our analysis; the potential theory

(PT) method first introduced in Hubbard (1999), and the more recently-developed concentric Maclaurin spheroid method (CMS; Hubbard, 2013), which we take as our benchmark for precision solutions for a differentially rotating barotrope. We then perform a three-way comparison between these two barotropic methods and the thermal wind method (TW), which can model any wind structure. One of the main goals of this study is to investigate the errors introduced in the TW calculation due to the sphericity assumption. The good agreement between the TW and the barotropic models, particularly the more stable and precise CMS method, indicates that the effect of oblateness on the dynamically induced gravity harmonics is not large. To extend this initial tentative conclusion, in a forthcoming paper we present a fully consistent generalization of the TW method that makes no assumptions concerning the shape of the planet (Galanti et al., 2016). While this generalized method is far more computationally intensive, we shall find that it provides only small modifications to the simple spherical TW.

Therefore, this study provides a benchmark for comparison of different methods for calculating the gravity harmonics resulting from internal dynamics. Results presented here are also consistent with the method of Wisdom (Wisdom and Hubbard, 2016). Although the barotropic limit provides a good reference for model comparison, it is far from a realistic picture of the dynamics of the interior. Thermal-wind type models provide opportunities for a much wider range of solutions, including profiles that have various types of vertical shear in the flow structure, and including north-south asymmetries that result in odd gravity harmonics. As the odd gravity harmonics will likely be purely from dynamics (the solid-body odd signal is identically zero), they will be advantageous in characterizing the wind structure without the need to disentangle the dynamical signal from the solid-body one (Kaspi, 2013). Identifying J_3, J_5 etc. might be one of the first results to emerge from the Juno and Cassini gravity measurements. Another possibility is that the interior structure is completely decoupled from the cloud-level wind structure. In that case, more complex flow models will be necessary, but as we expect any type of large scale flow on a rapidly rotating giant planet to be to leading order in geostrophic balance, thermal-wind type models can be useful for this type of analysis.

Acknowledgments

We acknowledge the Kupcinet-Getz International Science School at the Weizmann Institute of Science (WIS) for providing support for J. Davighi's work at the WIS during the summer of 2013, which led to the majority of this study. Y.K. and E.G. acknowledge support from the Israeli Ministry of Science (grant 45-851-641), the Minerva foundation with funding from the Federal German Ministry of Education and Research, and from the Helen Kimmel Center for Planetary Science at the WIS. W.B.H. and Y.K. acknowledge support by the Juno project.

References

Atkinson, D.H., Pollack, J.B., Seiff, A., 1996. Galileo doppler measurements of the deep zonal winds at Jupiter. Science 272, 842–843.
Aurnou, J.M., Olson, P.L., 2001. Strong zonal winds from thermal convection in a rotating spherical shell. Geophys. Res. Lett. 28 (13), 2557–2559.
Bolton, S.J., 2005. Juno Final Concept Study Report. Technical Report, AO-03-OSS-03. New Frontiers, NASA.
Busse, F.H., 1976. A simple model of convection in the jovian atmosphere. Icarus 29, 255–260.
Busse, F.H., 1994. Convection driven zonal flows and vortices in the major planets. Chaos 4 (2), 123–134.
Cao, H., Stevenson, D. J., 2015. Gravity and zonal flows of giant planets: From the euler equation to the thermal wind equation. arXiv:1508.02764.
Chan, K.L., Mayr, H.G., 2013. Numerical simulation of convectively generated vortices: Application to the jovian planets. Earth Planet. Sci. Lett. 371, 212–219.
Cho, J., Polvani, L.M., 1996. The formation of jets and vortices from freely-evolving shallow water turbulence on the surface of a sphere. Phys. Fluids. 8, 1531–1552.
Choi, D.S., Showman, A.P., 2011. Power spectral analysis of Jupiter's clouds and kinetic energy from Cassini. Icarus 216, 597–609.
Christensen, U.R., 2002. Zonal flow driven by strongly supercritical convection in rotating spherical shells. J. Fluid Mech. 470, 115–133.
Conrath, B.J., Flasar, F.M., Pirraglia, J.A., et al., 1981. Thermal structure and dynamics of the jovian atmosphere. II - Visible cloud features. J. Geophys. Res. 86, 8769–8775.
Dowling, T.E., Ingersoll, A.P., 1988. Potential vorticity and layer thickness variations in the flow around Jupiter's great red spot and white oval BC. J. Atmos. Sci. 45 (8), 1380–1396.
Dowling, T.E., Ingersoll, A.P., 1989. Jupiter's great red spot as a shallow water system. J. Atmos. Sci. 46 (21), 3256–3278.
Durran, D.R., 1989. Improving the anelastic approximation. J. Atmos. Sci. 46, 1453–1461.
Finocchiaro, S., Iess, L., 2010. Numerical simulations of the gravity science experiment of the Juno mission to Jupiter. In: Spaceflight Mechanics. American Astronomy Society, pp. 1417–1426.
Galanti, E., Kaspi, Y., 2016. An adjoint based method for the inversion of the Juno and Cassini gravity measurements into wind fields. Astrophys. J. 820, 91.
Galanti, E., Kaspi, Y., Tziperman, E., 2016. A full, self-consistent, treatment of thermal wind balance on oblate fluid planets. Submitted.
Gastine, T., Wicht, J., Aurnou, J.M., 2013. Zonal flow regimes in rotating anelastic spherical shells: An application to giant planets. Icarus 225, 156–172.
Gierasch, P.J., Magalhaes, J.A., Conrath, B.J., 1986. Zonal mean properties of Jupiter's upper troposphere from Voyager infrared observations. Icarus 67, 456–483.
Glatzmaier, G., 2014. Self-consistent predictions of the gravity and magnetic fields to be measured by Juno at Jupiter. In: AGU Fall Meeting Abstracts, A3971.
Guillot, T., 2005. The interiors of giant planets: Models and outstanding questions. Ann. Rev. Earth Plan. Sci. 33, 493–530.
Guillot, T., Morel, P., 1995. CEPAM: A code for modeling the interiors of giant planets. Astron. Astro. Supp. Ser. 109, 109–123.
Heimpel, M., Aurnou, J., Wicht, J., 2005. Simulation of equatorial and high-latitude jets on Jupiter in a deep convection model. Nature 438, 193–196.
Hubbard, W.B., 1975. Gravitational field of a rotating planet with a polytropic index of unity. Soviet Astron. 18, 621–624.
Hubbard, W.B., 1982. Effects of differential rotation on the gravitational figures of Jupiter and Saturn. Icarus 52, 509–515.
Hubbard, W.B., 1984. Planetary Interiors. Van Nostrand Reinhold Co., New York, p. 343.
Hubbard, W.B., 1999. Note: Gravitational signature of Jupiter's deep zonal flows. Icarus 137, 357–359.
Hubbard, W.B., 2012. High-precision Maclaurin-based models of rotating liquid planets. Astrophys. J. Let. 756, L15.
Hubbard, W.B., 2013. Conventric maclaurian spheroid models of rotating liquid planets. Astrophys. J. 768 (1).
Hubbard, W.B., Schubert, G., Kong, D., et al., 2014. On the convergence of the theory of figures. Icarus 242, 138–141.
Hubbard, W.B., Slattery, W.L., Devito, C.L., 1975. High zonal harmonics of rapidly rotating planets. Astrophys. J. 199, 504–516.
Iess, L., Stevenson, D.J., Parisi, M., et al., 2014. The gravity field and interior structure of Enceladus. Science 344, 78–80.
Jacobson, R. A., 2003. JUP230 Orbit Solutions. http://ssd.jpl.nasa.gov/.
Jones, C.A., Kuzanyan, K.M., 2009. Compressible convection in the deep atmospheres of giant planets. Icarus 204, 227–238.
Kaspi, Y., 2013. Inferring the depth of the zonal jets on Jupiter and Saturn from odd gravity harmonics. Geophys. Res. Lett. 40, 676–680.
Kaspi, Y., Flierl, G.R., 2007. Formation of jets by baroclinic instability on gas planet atmospheres. J. Atmos. Sci. 64, 3177–3194.
Kaspi, Y., Flierl, G.R., Showman, A.P., 2009. The deep wind structure of the giant planets: Results from an anelastic general circulation model. Icarus 202, 525–542.
Kaspi, Y., Hubbard, W.B., Showman, A.P., et al., 2010. Gravitational signature of Jupiter's internal dynamics. Geophys. Res. Lett. 37, L01204.
Kaspi, Y., Showman, A.P., Hubbard, W.B., et al., 2013. Atmospheric confinement of jet-streams on Uranus and Neptune. Nature 497, 344–347.
Kong, D., Zhang, K., Schubert, G., 2012. On the variation of zonal gravity coefficients of a giant planet caused by its deep zonal flows. Astrophys. J. 748.
Lian, Y., Showman, A.P., 2010. Generation of equatorial jets by large-scale latent heating on the giant planets. Icarus 207, 373–393.
Liu, J., 2006. Interaction of Magnetic Field and Flow in the Outer Shells of Giant Planets. California Institute of Technology Ph.D. thesis.
Liu, J., Goldreich, P.M., Stevenson, D.J., 2008. Constraints on deep-seated zonal winds inside Jupiter and Saturn. Icarus 196, 653–664.
Liu, J., Schneider, T., 2010. Mechanisms of jet formation on the giant planets. J. Atmos. Sci. 67, 3652–3672.
Liu, J., Schneider, T., Fletcher, L.N., 2014. Constraining the depth of Saturn's zonal winds by measuring thermal and gravitational signals. Icarus 239, 260–272.
Liu, J., Schneider, T., Kaspi, Y., 2013. Predictions of thermal and gravitational signals of Jupiter's deep zonal winds. Icarus 224, 114–125.
May, J., Carr, T.D., Desch, M.D., 1979. Decametric radio measurement of Jupiter's rotation period. Icarus 40, 87–93.
Orton, G.S., Fisher, B.M., Baines, K.H., et al., 1998. Characteristics of the Galileo probe entry site from Earth-based remote sensing observations. J. Geophys. Res. 103, 22791–22814.
Parisi, M., Galanti, E., Finocchiaro, S., et al., 2016. Probing the depth of Jupiter's great red spot with the juno gravity experiment. Icarus 267, 232–242.

Pedlosky, J., 1987. Geophysical Fluid Dynamics. Springer-Verlag, p. 710.
Porco, C.C., West, R.A., McEwen, A., et al., 2003. Cassini imaging of Jupiter's atmosphere, satellites and rings. Science 299, 1541–1547.
Rhines, P.B., 1975. Waves and turbulence on a beta plane. J. Fluid Mech. 69, 417–443.
Rhines, P.B., 1979. Geostrophic turbulence. Ann. Rev. Fluid Mech. 11, 401–441.
Riddle, A.C., Warwick, J.W., 1976. Redefinition of System III longitude. Icarus 27, 457–459.
Sánchez-Lavega, A., Pérez-Hoyos, S., Rojas, J.F., et al., 2003. A strong decrease in Saturn's equatorial jet at cloud level. Nature 423, 623–625.
Sánchez-Lavega, A., Rojas, J.F., Sada, P.V., 2000. Saturn's zonal winds at cloud level. Icarus 147, 405–420.
Scott, R.K., Polvani, L.M., 2007. Forced-dissipative shallow-water turbulence on the sphere and the atmospheric circulation of the giant planets. J. Atmos. Sci. 64, 3158–3176.
Showman, A.P., 2007. Numerical simulations of forced shallow-water turbulence: effects of moist convection on the large-scale circulation of Jupiter and Saturn. J. Atmos. Sci. 64, 3132–3157.
Showman, A.P., Dowling, T.E., 2000. Nonlinear simulations of Jupiter's 5-micron hot spots. Science 289, 1737–1740.
Showman, A.P., Gierasch, P.J., Lian, Y., 2006. Deep zonal winds can result from shallow driving in a giant-planet atmosphere. Icarus 182, 513–526.
Spilker, L. J., Altobelli, N., Edgington, S. G., 2014. Surprises in the Saturn system: 10 years of Cassini discoveries and more excitement to come. In: AGU Fall Meeting Abstracts, A1.
Taylor, G.I., 1923. Experiments on the motion of solid bodies in rotating fluids. R. Soc. Lond. Proc. Ser. A 104, 213–218.
Vasavada, A.R., Showman, A.P., 2005. Jovian atmospheric dynamics: An update after Galileo and Cassini. Rep. Prog. Phys. 68, 1935–1996.
Wicht, J., Jones, C.A., Zhang, K., 2002. Instability of zonal flows in rotating spherical shells: An application to Jupiter. Icarus 155, 425–435.
Williams, G.P., 1978. Planetary circulations: 1. Barotropic representation of the jovian and terrestrial turbulence. J. Atmos. Sci. 35, 1399–1426.
Williams, G.P., 1979. Planetary circulations: 2. The jovian quasi-geostrophic regime. J. Atmos. Sci. 36, 932–968.
Williams, G.P., 2003. Jovian dynamics. part 3: Multiple, migrating and equatorial jets. J. Atmos. Sci. 60, 1270–1296.
Wisdom, J., Hubbard, W.B., 2016. Differential rotation in Jupiter: A comparison of methods. Icarus 267, 315–322.
Zhang, K., Kong, D., Schubert, G., 2015. Thermal-gravitational wind equation for the wind-induced gravitational signature of giant gaseous planets: Mathematical derivation, numerical method and illustrative solutions. Astrophys. J. 806, 270–279.